Sequential Fe Reduction, Involving Two Different Fe^{+} Intermediates, in the Conversion Reaction of Prussian Blue in Lithium-Ion Batteries

María José Piernas Muñoz, [a, b, c, *] *Elizabeth Castillo-Martínez,* [a, d, *] *Eider Goikolea,* [a, e] *Pablo Blanco,* [a] *Estíbaliz Legarra,* [f] *José Javier S. Garitaonandia,* [g] *Soojeong Kim,* [b] *Timothy T. Fister,* [b] *Christopher S. Johnson,* [b] *Teófilo Rojo* [a, e]

[a] CICenergigune, Parque Tecnológico de Álava, Albert Einstein 48, ED. CIC, 01510 Miñano (Álava), SPAIN.

[b] Chemical Sciences and Engineering Division, Argonne National Laboratory, 9700 S Cass Ave., Lemont, IL 60439, USA.

[c] Present address: Inorganic Chemistry Department, University of Murcia, C/Campus Universitario 5, 30100 Murcia, SPAIN. mjpiernas@um.es

[d] Present address: Department of Chemistry, Complutense University of Madrid, Plaza de las Ciencias 2, 28040 Madrid, SPAIN. ecastill@ucm.es

[e] Present Address: Organic and Inorganic Chemistry Department, Basque Country University (UPV/EHU), Barrio Sarriena s/n, 48940 Leioa (Bilbao), SPAIN.

[f] BC Materials, Basque Center for Materials Applications and Nanostructures, Barrio Sarriena s/n, 48940 Leioa (Bilbao), SPAIN.

[g] Applied Physics II Department, Science and Technology Faculty, Basque Country University (UPV/EHU), Barrio Sarriena s/n, 48940 Leioa (Bilbao), SPAIN.

ABSTRACT

Ex-situ X-ray Absorption Spectroscopy and *in operando* ^{57}Fe-Mössbauer spectroscopic measurements are conducted to examine in detail the ongoing reaction mechanism of potassium Prussian blue (K-PB) within the narrow [1.6 – 0.005 V] voltage range, and so to determine whether this material truly undergoes a conversion reaction, as we proposed elsewhere. The generation of Fe^0 is confirmed by both techniques, finding that 40 to 58% of iron gets reduced to metallic iron at 5 mV. The elucidation of the mechanism by *in-situ* ^{57}Fe-Mössbauer further reveals a sequential process for the reduction (lithiation) of the two different iron species initially present in Prussian blue. Both, HS (high spin) Fe^{2+}-N first, and LS (low spin) Fe^{II}-C next, go through the unusual $Fe^{1+/I}$ formal oxidation state during the reduction process, before forming surface Fe^0 nanoparticles (NPs) below 0.48 V. Upon charge, Fe^0 NPs preferentially oxidizes into Fe^+-N. Interestingly, these surprising Fe^+ species play an important role in decreasing the overpotential during the charge (delithiation) process with respect to other conversion systems.

INTRODUCTION

Li-ion batteries (LIBs hereafter) are an essential electrochemical energy storage (EES) technology in industry and everyday life,[1, 2, 3] as they combine both high energy density and power density.[4, 5] Although the most exploited intercalation cathodic materials for LIBs are layered oxides, spinel-type oxides and polyanionic compounds, [5, 6] the anodic material par excellence to date is graphite.[7] However, high capacity alternative materials that react through conversion reactions, and especially those based on abundant Fe have attracted the attention of battery researchers. [8, 9]

In the last decade, several groups have explored the electrochemical performance of Prussian Blue Analogues (PBAs) as possible new anode materials for LIBs. PBAs are a family of compounds with molecular formula $AM[M'(CN)_6]\cdot nH_2O$, where A is typically an alkali ion (Li^+, Na^+, K^+), M and M' are transition metals, sometimes M = M', and commonly M' = Fe. [10, 11, 12] They present a 3D structure where M'^{II} and M^{3+} occupy alternate corners of a simple cubic framework bridged by linear μ-(C≡N)- anions (see **Figure 1**a). [12, 13] The linear (C≡N)- ligand gives a M^{3+}–N≡C– M'^{II} bond length of about 5 Å, thus creating open channels that allow A^+ ions to be reversibly inserted. [13, 14] Please note here (and hereafter) the distinct notation used for the two types of iron present in the complex. We have followed Mössbauer spectroscopists' notation. That is, roman numerals are used for LS Fe covalently bonded to C, while regular numbers are reserved for more ionic N-bonded HS Fe.

The first investigations of PBAs as anodes for non-aqueous LIBs were conducted in 2013 by Shokouhimehr et al. [15] Cobalt hexacyanoferrate NPs, $KCo[Fe(CN)_6]\cdot zH_2O$, were evaluated in the voltage range [3.0, 0.01] V vs. Li^+/Li, displaying a reversible charge capacity of 544 mA h g^{-1} at current densities of 100 m Ag^{-1}. In 2014, Nie and coworkers tested $Co_3[Co(CN)_6]_2$ nanocubes in

the same potential range. [16] The specific charge capacity delivered was 294 mA h g^{-1} at 20 mA g^{-1}, which the authors speculated to be result of the oxidation of three redox couples: C-$Co^{I/II}$, C-$Co^{II/III}$, and N-$Co^{II/III}$. It is important to note here that we are adopting the half-cell electrochemical criterion. Hence, with oxidation (or charge), we refer to the anode oxidation vs. lithium metal plating, i.e., anode delithiation. In 2015, Xiong and collaborators [17] showed that $Mn^{3+}[Fe^{II}(CN)_6]_{0.6667}\cdot 5H_2O$ cubes exhibited a first charge capacity of 545 mA h g^{-1}, also in the [3.0, 0.01] V vs. Li^+/Li range, at a current density of 200 mA g^{-1}. In these three works, the enormous first discharge capacity observed for PBAs was just attributed to the formation of the solid electrolyte interphase (SEI) and the reduction (lithiation) of the material via an intercalation mechanism. Nevertheless, our findings suggested another explanation.

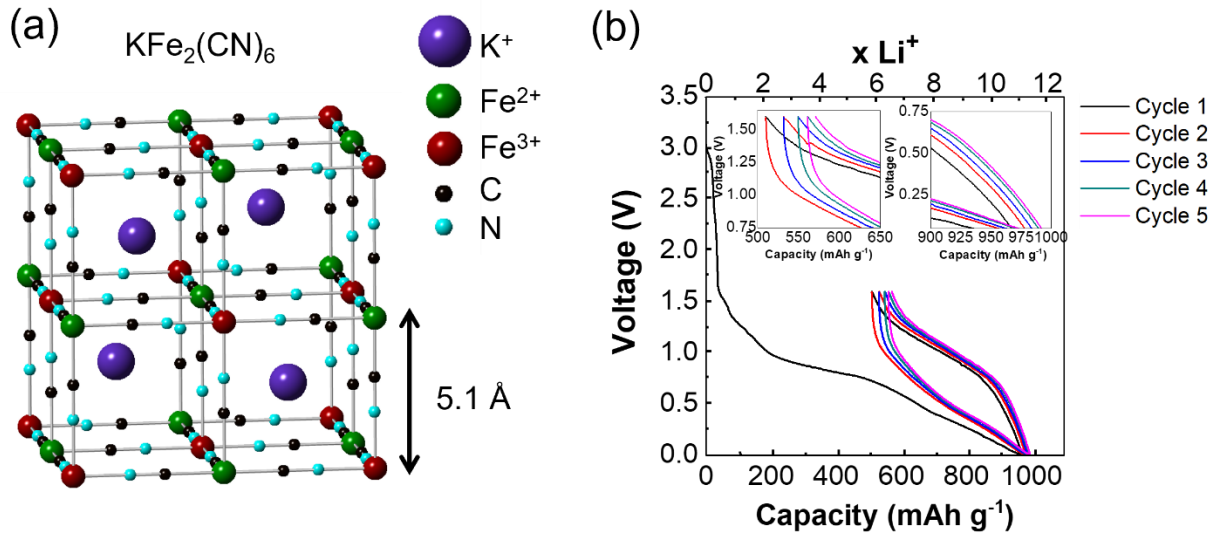

Figure 1. (a) Prussian Blue structure, (b) Voltage profile of the five first galvanostatic cycles of Prussian Blue when tested vs. lithium with 1 M $LiPF_6$ in ethylene carbonate: dimethyl carbonate (EC: DMC) at C/10.[18] To facilitate the reader´s comparison among cycles, enlarged areas of the end of charge and discharge are shown in the insets of the voltage profile.

In 2014, we reported the electrochemical performance of (all iron) Prussian Blue $K_{1-x}Fe_{2+x/3}(CN)_6 \cdot 2.73H_2O$ (x = 0.12) NPs as anode.[18] The material exhibited a large first discharge capacity (ca. 1000 mA h g^{-1}) and a plateau below 0.9 V, with high reversible capacities close to 450 mA h g^{-1} at 8.75 mA g^{-1} (**Figure 1**b), being also capable of retaining up to 350 mA h g^{-1} after 50 cycles (what took ca. 6 months of cycling), in the attractive voltage window of 1.6 - 0.005 V vs. Li^+/Li. Since such reversible capacities were far higher than the theoretically expected for the insertion of 2 Li^+ per formula unit via common intercalation mechanism (175 mA h g^{-1}), we performed a series of *ex-situ* experiments (powder X-ray diffraction (PXRD), infrared (FTIR), and transmission electron microscopy (TEM/STEM)) to elucidate the mechanism of reaction. Based on them, we proposed, for the first time for this type of material, a conversion (or displacement) reaction, involving the formation of metallic Fe^0 NPs [18] along the first discharge (as Equation (**1**) illustrates):

$$KFe^{3+}[Fe^{II}(CN)_6]\cdot yH_2O \xrightarrow[+\,e^-]{+\,Li^+} LiKFe^{2+}[Fe^{II}(CN)_6]\cdot yH_2O \xrightarrow[+\,4e^-]{+\,4Li^+} 2\,Fe^0 + 5\,LiCN + KCN \qquad (\mathbf{1})$$

Simultaneously, other lithium derivatives, such as LiF or LiOH, were formed. These would accordingly result from the decomposition of the electrolyte salt ($LiPF_6 \rightarrow LiF\,(s) + PF_5\,(g)$), or from the reaction of the water present in the structure of K-PB with the lithium salt composing the electrolyte. Equation (**1**) is a simplified equation that does not consider the $[Fe^{II}(CN)_6]^{4-}$ vacancies of Prussian Blue. For a major completeness, please see our previous work. [18]

Through the so-called conversion reaction (as shown in Equation (**2**)), which is often impressively reversible (⇆), materials can incorporate more than 1 Li^+/T.M. (T.M. = transition metal), as they get reduced from M^{y+} to metallic M^0 NPs, while undergoing a complete structural change. [3, 19]

Understanding their mechanism of reaction can help us to design materials that undergo highly reversible conversion reactions.

$$M_xX_y + n\ yLi^+ + 2e- \leftrightarrow yLi_nX + xM \quad (\mathbf{2})$$

Subsequent studies still reported some contradictory results regarding the mechanism of reaction of PBAs [20, 21, 22, 23] when tested at low voltages against metallic lithium. For instance, based on lab XRD data, Chen et al. [20] suggested that $Ti_xFe_{2-x}(CN)_6 \cdot 2H_2O$ also followed a conversion reaction, as described by Equation (**3**):

$$Ti_xFe_{2-x}(CN)_6 + 6\ Li^+ + 6\ e^- \leftrightarrows x\ Ti + (2-x)\ Fe + 6\ LiCN \quad (\mathbf{3})$$

Whereas, based on *ex-situ* XRD and synchrotron X-ray Absorption Spectroscopy (XAS), the reversible capacity of $Na_{1.34}Mn[Fe(CN)_6]_{0.84} \cdot 3.4H_2O$ (Mn-PBA) thin films was ascribed to the conversion reaction of electrochemically formed α-Fe_2O_3 (Eq. (**4**)) [21], the storage mechanism of the potassium analogue $K_{1-x}Mn_{1+x/2}[Fe(CN)_6] \cdot yH_2O$ was simply attributed to the intercalation/de-intercalation of Li^+ along with the redox reaction of Fe^{3+} to Fe^{2+}, with no major structural change. [22] However, even if Mn^{2+} was reduced to Mn^{+1} as reported by Cui and cols.[24], the large reversible capacity (> 300 mA h g^{-1}) cannot be explained by reversible intercalation only, unless Fe also gets reduced below the 2+ oxidation sate. Nonetheless, the existence of -C≡N- coordinated Fe^{+1} species has not been reported to occur in battery materials.

$$Fe_2O_3 + 6Li^+ + 6e^- \leftrightarrows 2Fe + 3\ Li_2O \quad (\mathbf{4})$$

Since reversible capacities on the order of 700 mA h g^{-1} were achieved at 30 mA g^{-1} with $Fe_4(Fe(CN)_6)_3$, of which up to 548 mA h g^{-1} were retained at current densities of 215 mA g^{-1} (about 2.4C) after 550 cycles [23], and hysteresis between charge and discharge (~0.5 V) is considerably

decreased vs. other Fe-based conversion materials (0.9-1.2 V) for iron oxides [25] and iron fluorides [26], implementation of this electrode material seems desirable if a better understanding of the materials reaction mechanism can be achieved.

Despite our *ex-situ* experiments in $K_{0.88}Fe_{2.04}(CN)_6 \cdot 2.73H_2O$ suggested the occurrence of a conversion reaction (because of the loss of Fe-CN stretching in FTIR, the irreversible disappearance of PB reflections in the PXRD pattern along with the detection of bright NPs in the STEM of fully discharged electrodes), additional information from other techniques is necessary to track Fe oxidation states, confirm the formation of Fe^0 and understand the reaction mechanism in more detail. Nonetheless, since Fe^0 NPs are highly reactive in contact with air, *in-situ*, or even *in operando* measurements seem necessary. Although *in-situ* or *in operando* experiments are becoming increasingly common for investigating the evolution of electrochemical systems along the cycling process, especially for XRD, *in-situ* or *in operando* Mössbauer [27, 28, 29, 30, 31, 32] studies, which are specific to few nuclei such as Fe or Sn, are still scarce and especially valuable here.

In the present work, *ex-situ* XAS and *in operando* Mössbauer measurements were conducted to elucidate the reaction mechanism and determine whether Fe^0 NPs were generated during the electrochemical reduction of Prussian Blue in the narrow voltage window [1.6 – 0.005] V vs. Li^+/Li. Given the reversibility of the reaction within the selected voltage range, even though small capacity losses occur from one cycle to another, only the first cycle - or the first cycle and a half - is evaluated.

EXPERIMENTAL SECTION

Prussian Blue synthesis. Potassium Prussian Blue, $K_{1-x}Fe_{1+x/3}[Fe(CN)_6]\cdot yH_2O$, was synthesized following the simple co-precipitation method described in our previous work. [18] Basically, 100 mL of an aqueous solution 40 mM of $K_4[Fe(CN)_6]\cdot 3H_2O$ were added to another 100 mL of an aqueous solution 40 mM containing $FeCl_3\cdot 6H_2O$, forming a colloidal suspension of "soluble" Prussian Blue. After subjecting the suspension to a process of centrifugation and filtration, washing the resulting precipitate with de-ionized H_2O (3 x 10 ml) and ethanol (3 x 10 ml) and subsequently drying it under vacuum, the dark blue product was isolated.

Physicochemical Characterization.

PXRD data were collected in the range $2\theta = 5^{\circ}$ to 80°, with a step width of 0.0194°, operating a Bruker D8 Advance X-Ray diffractometer ($\lambda_{CuK\alpha}$ = 1.54056 Å). TGA NETZSCH STA 449 F3 Jupiter allowed to record the thermogravimetric curve of Prussian Blue within the temperature range from 30 to 325 ºC, at a temperature step of 10 K min^{-1}, under N_2 atmosphere. SEM images were taken in a Quanta 200 FEG (FEI) scanning electron microscope, at an operating potential of 20 kV. XPS spectra were acquired in transmission mode with pass energy of 20 eV in an UHV system equipped with a hemispherical electron energy analyzer PHOIBOS 150 (SPECS) and a twin Al/Mg anode – X-ray source XR50 (SPECS) operated at 12 keV and a power of 100 W. The size of the acceptance area of the analyzer were was ca. 2 mm in diameter and its energy scale was calibrated against Cu $2p_{3/2}$, Ag $3d_{5/2}$ and Au$4f_{7/2}$ lines of standard Au-Ag-Cu sample.

X-ray absorption near-edge structure (XANES) region of X-ray absorption spectroscopy (XAS) is especially sensitive to the formal oxidation state of a particular element. [33] XAS measurements at the Fe K-edge were performed at the MRCAT (10-BM) beamline at the Advanced Photon Source

(APS), in Argonne National Laboratory. To calibrate energy, an iron metal foil was measured downstream from the sample as a reference and for energy calibration. Absorption spectra were collected in transmission mode, using homogeneous electrodes with less than 0.1 mg difference in their active material mass loading to thereby ensure their comparability. Prior to XAS measurements, those electrodes were cycled in half cells vs. Li^+/Li and stopped at different stages of the electrochemical curve. Each XAS scan took about 25 minutes, covering an energy range from -300 eV below the edge to 900 eV above the edge (~ 6800 - 8000 eV). Due to the disordered, multisite nature of the conversion reaction, XANES data were primarily analyzed, although EXAFS data were also extracted. XAS data were processed and analyzed using Athena and Artemis software packages. [34]

^{57}Fe-Mössbauer spectroscopy is another valuable technique when dealing with changes in the oxidation state of iron, as well as its coordination environment. [35] Mössbauer hyperfine parameters, *i.e.*, the isomer shift (δ) and quadrupole splitting (Δ), extracted from fitting experimental patterns are usually sufficient to identify the valence state of Fe and its chemical environment. ^{57}Fe-Mössbauer measurements were conducted at room temperature at the UPV/EHU, in the velocity range from - 4.5 to 4.5 mm s^{-1} and in transmission geometry, using a spectrometer provided with a 25 mCi ^{57}Co–Rh source. The velocity was calibrated using the magnetic six-line spectrum of a high-purity iron foil absorber. The values of the isomer shift (δ) are given with respect to reference *bcc* (body centered cubic) Fe and the spectra were fitted with the NORMOS fitting Program. [36]

In-situ Mössbauer spectra were recorded every 15 minutes, i.e., at time 0, 15, 30 min and so on, during the first discharge and the first charge of Prussian Blue against metallic lithium. The corresponding voltage for each Mössbauer spectrum was obtained from the voltage profile electrochemical curve (Voltage (V) vs. time), here not shown. To enable simultaneous ^{57}Fe-

Mössbauer and electrochemical data collection, a new *in-situ* Mössbauer cell was designed and built at CIC EnergiGUNE. Inside the cell, the cathode/separator/anode sandwich was assembled as in a conventional coin-type cell. A VSP potentiostat (BioLogic) was the instrument used to perform the electrochemical experiment.

Solid State Nuclear Magnetic Resonance (ss NMR) data were collected on a Bruker 500 MHz spectrometer, with a 1.3 mm probe. Rotors were spun at a magic-angle-spinning (MAS) rate of 50 kHz and spectrum collected at 73.6 MHz (^{6}Li) and 470 MHz (^{19}F) with a rotor synchronized Hahn echo sequence (90°-τ-180°-τ-acq.), with a 90° pulse of 3.6 μs (^{19}F, ^{6}Li) and a recycle delay of 1s (^{6}Li) and 40 s (^{19}F). Spectra are referenced to 0.1M LiCl and secondary LiF (−201 ppm) [37]. Approximately 100 000 scans were collected for each ^{6}Li and ^{19}F ss NMR spectrum.

ss NMR was collected *ex-situ* on an electrode, containing 80 wt% of active material and 20 wt % super C-65® carbon, after cycling them till the end of discharge (0.005 V vs. Li^{+}/Li). After cell disassembly inside a glovebox with O_2 and H_2O levels less than 0.5 ppm, the electrode was washed with dimethyl carbonate twice, dried under vacuum and packed into rotors.

Electrochemical Characterization.

Electrochemical measurements prior to XAS data collection. Prussian Blue was electrochemically cycled against lithium in a battery and cell test equipment (MACCOR Series 4000 Battery Tester). Galvanostatic tests between 0.005 V and 1.6 V vs. Li^{+}/Li were conducted at room temperature, using coin-type half cells (CR2032) and a CC-CV (constant current - constant voltage) protocol. Working electrodes were prepared by mixing K-PB with super C-65® and polyvinylidene fluoride (PVDF) dissolved in N-methylpyrrolidone in an 80:10:10 ratio. After coating the resulting slurry over Cu foil, drying the laminate under vacuum at 80°C overnight and calendaring it, 13 mm

diameter electrodes were punched. Typical cell loadings were 8.5 mg of active material per coin cell. A lithium metal disk was used as counter and reference electrode and a glass fiber filter paper (Whatman, GF-B) impregnated with commercial (Solvionic) 1M $LiPF_6$ in ethylene carbonate: dimethyl carbonate (EC: DMC) was used as separator. The current density was fixed to 1C, based on the theoretical capacity of $C_{PB,\,th}$ = 87.5 mA h g^{-1} corresponding to the insertion of 1 Li^+/formula unit (f.u.).

For the *ex-situ* XAS synchrotron measurements, the K-PB electrodes were stopped at different voltage values of the electrochemical curve (first discharge-charge and second discharge). Then, the cells were disassembled inside of an Ar-filled glove box with O_2 and H_2O levels less than 0.5 ppm. The electrodes were thoroughly rinsed several times with DMC to remove the excess of electrolyte residue and were dried at 80˚C overnight. Afterwards, the electrodes were sealed with aluminum-coated Mylar® to create an air- and water-protective barrier. Finally, each electrode was placed inside an aluminized pouch bag that was sealed also to prevent their possible reaction with O_2 while transporting it to the synchrotron facilities. It is important to note that the electrodes were kept for ca. 24 h inside the glove box, before XAS data collection.

Electrochemical in-situ measurements coupled to ^{57}Fe-Mössbauer. At the fixed current density of 1C and at room temperature, the voltage curves of potassium Prussian Blue were recorded between 0.005 V and 1.6 V vs. Li^+/Li using a VSP potentiostat and the *in-situ*/*in operando* Mössbauer cell.

In this case, self-standing laminates were prepared by dispersing 70 wt. % of K-PB with 20 wt. % of conductive carbon (Super C-65®) and 10 wt. % of teflon (PTFE, from a 60 wt. % aqueous dispersion, Sigma-Aldrich) in ethanol. Then, self-standing electrodes of 16 mm diameter were punched and dried under vacuum at 80 ºC overnight, with a mass loading of approximately 40 mg

of active material per electrode. The utilization of self-standing electrodes had here a dual purpose. On the one hand, avoiding the Cu current collector allows increasing the intensity of the γ-rays transmitted through the sample. On the other hand, self-standing electrodes were several times thicker than the typical laminated electrodes and the higher Fe content enhanced the Mössbauer signal. In fact, several tests with different mass loadings were previously performed in order to assess which sample thickness allowed to achieve the optimum relative absorption of the Mössbauer signal experimentally.

RESULTS AND DISCUSSION

PXRD confirmed the formation of K-PB. As it can be observed in **Figure 2**a, its diffraction pattern coincides with that reported for the material, [38] which adopts cubic symmetry and space group *Fm*-3*m*. The broad reflections are a consequence of the nanometric crystal size. According to thermal analysis, two different weight losses associated to physiosorbed and zeolitic water were detected at 80 and 125 ºC, respectively, resulting in a total of 2.73 H_2O molecules per formula unit (see **Figure S1**a). The aggregation of K-PB nanometric domains into larger microparticles, forming agglomerates from 1 to 50 μm particle size, can be observed on SEM images (**Figure S1**b and c).

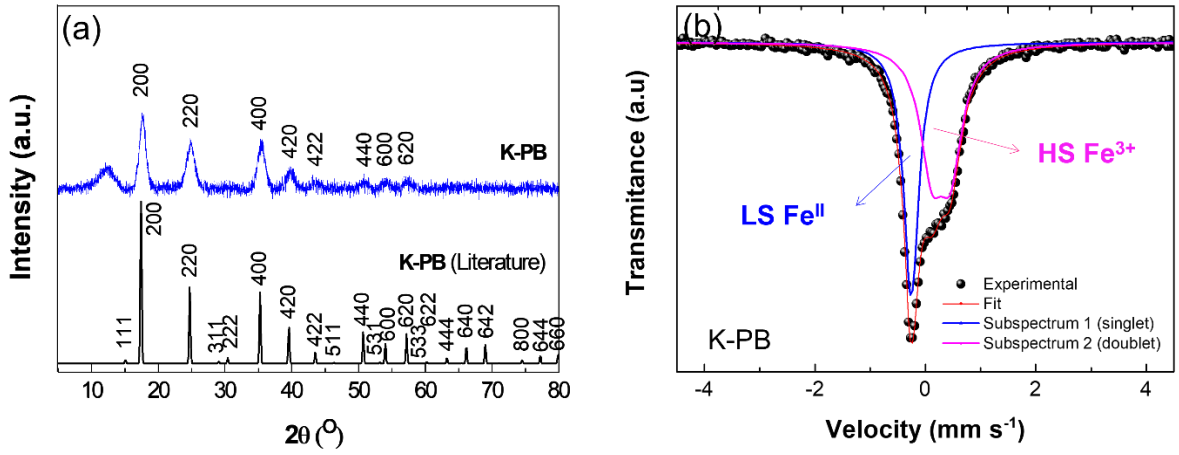

Figure 2. (a) PXRD patterns of K-PB synthesized and K-PB listed in the ICSD Karlsruhe Database (162081) [18]. Note that the peak below 2θ = 15º is due to the Kapton film used. b) Mössbauer spectrum of K-PB. Experimental (black dots) and fitting (red line) are shown along with the blue and pink solid lines that represent the LS Fe^{II} and HS Fe^{3+} spectral components, respectively.

The ^{57}Fe-Mössbauer spectrum of the as-produced pristine material (see **Figure 2**b) was fitted using two signals corresponding to the two different types of iron present in Prussian Blue. A singlet attributed to low spin (LS) Fe^{II} covalently bonded to C and a doublet corresponding to high spin (HS) Fe^{3+} bonded to N, as expected for K-PB. Its hyperfine parameters are listed in **Table 1**, and are in good agreement with those encountered in the literature for this material. [39] An Fe^{3+}/Fe^{II} ratio of 1.33 was calculated, consistent with the 1.33 expected for a K-PB containing a 25% of $[Fe(CN)_6]^{4-}$ defects [38], typical in this type of compounds. XPS analysis at the Fe 2p edge (**Figure S1**d) additionally corroborates the two distinct types of iron species detected by ^{57}Fe-Mössbauer in the as-prepared material. Two split orbit components $2p_{3/2}$ and $2p_{1/2}$, in accordance with those previously reported for LS Fe^{II},[40, 41] are respectively observed at 709 and 722 eV; and a small peak, typically assigned to HS Fe^{3+},[41, 42] is distinguished at 713 eV.

Table 1. Isomer shift relative to body cubic centered (*bcc*) Fe (δ), quadrupolar splitting (Δ) and Fe atomic ratio values extracted from the ^{57}Fe-Mössbauer fitting for iron in K-PB.

Compound	Assignment	**δ** (mms^{-1})	**Δ** (mms^{-1})	**Fe %**
K-PB[a]	LS Fe^{II}	-0.15(1)	0	43
	HS Fe^{3+}	0.40(1)	0.34(1)	57

[a] $K_{1-x}Fe^{3+}_{(x+1/3)}[Fe^{II}(CN)_6]$

Ex-situ synchrotron XAS measurements were carried out in electrodes cycled in lithium half-cells, between 1.6 and 0.005 V, which were stopped at different voltage values (points i-ix) of the first discharge-charge and second discharge electrochemical curve, as **Figure 3**a illustrates.

The XANES region of the XAS spectra of K-PB electrodes stopped at different voltages during the first Li-insertion process is shown in **Figure 3**b. Point "i" corresponds to an electrode that was assembled in a half cell, to emulate the most similar conditions experienced by the rest of electrodes, but it was not subjected to electrochemistry, *i.e.*, it represents the OCV of the cell, at ca. 3.2 V vs. Li^+/Li. The energy of the main peaks in "i" at 7130 eV indicates that we initially had a mixture of Fe^{3+} and Fe^{2+}. A clear shift in the peak at 7130 eV towards lower energy is observed along the first discharge process (from point "i" to point "iv"). This shift down to 7128 eV is assigned to the reduction from Fe^{3+} to Fe^{2+}, as Prussian White (ideally $LiKFe^{2+}[Fe^{II}(CN)_6]$) is expected to form below 2 V vs. Li^+/Li, and it is accompanied by a decrease in its peak intensity for voltages below 1 V, as a result of a descent in its population due to the subsequent reduction of Fe^{2+}. It is also important to note the presence of a peak at ca. 7119 eV, whose intensity grows in the first stage of the reduction (from 3.2 V to 1.0 V) and then, at lower voltages, it vanishes. Conversely, the shoulder at 7113.7 eV augmented its intensity upon reduction to 0.5 V ("iii") and below, reaching its maximum at 5 mV (point "iv"). The pre-edge observed at 7113.7 eV probably

corresponds to the transition of the *1s* electron to an unoccupied e_g orbital of iron ions (1s → 3d), most likely from the LS Fe^{II}.[43] Although this electronic transition is dipole forbidden in an ideal octahedral environment, the distortion of the Prussian blue structure along the discharge may allow observing it. Alternatively or complementarily, a 3d-4p orbital mixing in distorted $[Fe(CN)_6]^{4-}$ or $[Fe(NC)_6]^{3-}$ octahedra could also be responsible for the low-energy pre-edge. This small pre-edge is even observed in the starting material, also probably for symmetry-breaking reasons due to undercoordinated Fe sites on the surface of K-PB NPs. In any case, the displacement of the edge to lower energies below 0.5 V indicates an iron reduction process,[43] which leads to metallic iron when approaching to 5 mV. Spectra iii – ix share multiple isosbestic points suggesting a two-phase mixture of spectrum ii and a reduced (Fe^0) phase. Fitting spectrum "iv" by linear combination analysis with an iron metal standard and spectrum "ii" confirmed the formation of Fe^0 at the totally discharged state (5 mV), indicating that at least 58% of the iron was reduced to Fe^0, while the remaining 42% corresponded to spectrum "ii" (which basically consists of Fe^{2+}). Such value of metallic iron (58%) is reasonable accounting the data reported, ca. 57% Fe^0 and 43% Fe^{2+}, for a totally discharged FeF_3 conversion cathode in a LIBs, [44] that was measured *ex-situ*. Our numbers are also somehow consistent with the 80% Fe metal and 20% $[Fe(CN)_6]^{4-}$ observed for $Na_{1.32}Mn[Fe(CN)_6]_{0.84}\cdot 3.4H_2O$ in its totally reduced state (at 10 mV) by XAS, when acting also as anode in LIBs. [21]

The trend is reverted upon oxidation (**Figure 3**c), i.e., the population of Fe^{2+} increases up to 80% for spectrum "vii" (charged to 1.6 V vs. Li^+/Li) and that of Fe^0 decreases down to 20%. Nonetheless, the intensity of the Fe^0 peak raises again in the following discharge (**Figure 3**d) while that of Fe^{2+} drops simultaneously, showing the reversibility to a big extent of this process within the [0.005 – 1.6] voltage range. Indeed, the XANES profile of spectra "ii", "vi" and "viii" are

almost identical (as **Figure S2** displays) and, likewise, spectra "iii", "v" and "ix" too, despite the population of Fe^{2+} is higher along the first discharge (point "iii"). Even though the peak intensity at spectrum "vii" (1.6 V) could look discordant, considering the intensity of its peaks with respect to those of electrodes stopped at 1.0 V ("vi" and "viii"), there is a reasonable explanation for this phenomenon. The spectrum was collected elapsed 2 weeks since the electrodes were prepared, what obviously contributed to its aging and subsequent decrease in the population of reduced species present in it, as these species will tend to evolve until reaching equilibrium. It is also important to note that, since we are not charging above 1.6 V vs. Li^+/Li, spectra of recharged states ("v – ix") do not show any sign of Fe^{3+}.

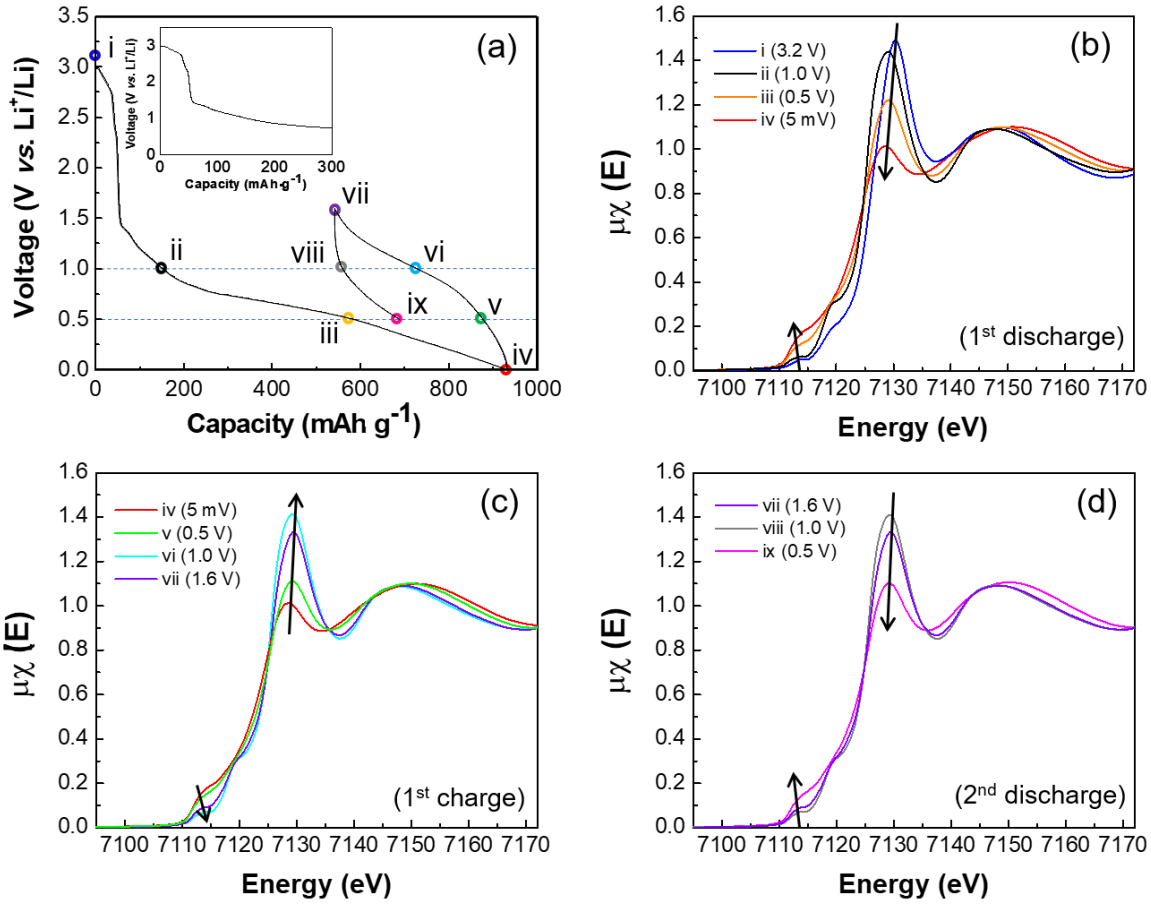

Figure 3. (a) First discharge-charge and second discharge voltage profile of K-PB vs. Li+/Li at room temperature when cycled at the voltage range of 0.005 - 1.6 V, reflecting the points at which the electrochemical reaction was stopped; and XAS spectra of K-PB at the Fe K-edge in the XANES region, respectively along (b) the first discharge, (c) first charge and (d) second discharge.

EXAFS interpretation resulted more complicated (see **Figure S3**). Fe-C (1.92 Å) and Fe-N (2.03 Å) distances [45] are too close to be able to distinguish between them, therefore, the EXAFS regions of these two iron sites interfere in a complicated manner. Besides, Fe-O distances, characteristic of water-related defects present in Prussian Blue, [45] are also reported in the 2 Å range, making even more difficult the assignment of the peaks. We attributed, hence, the constructive interferences in the 1 – 3 Å distance range (**Figure S3**b, spectrum i) to a first coordination sphere of Fe-C, Fe-N and Fe-O bonds and to a second coordination sphere of Fe-N-C or Fe-C-N. [46] The intensity of the 4-5 Å distance, corresponding to the third coordination sphere Fe-N-C-Fe is largely diminished with respect to what is found in larger particles. [47] Upon electrochemical reduction, the second coordination sphere seems to split. Little can be concluded from this splitting, which is more clearly observed at the lower voltages, when Fe^0 was already observed by XANES. What is certain is that the longer-range Fe-Fe distances at ca. 4.5 - 5 Å disappear along the first discharge and are not fully recovered in the subsequent cycle, thus indicating the partial rupture of the Prussian Blue structure and reinforcing the theory of the conversion/displacement mechanism.

In-situ Mössbauer spectra were continuously acquired throughout the different electrochemical cycling stages of K-PB vs. Li^+/Li, enabling to follow the Fe oxidation state evolution within the redox processes. As **Figure S4**a illustrates, the electrochemical performance obtained with the *in-situ* cell is comparable to that achieved using conventional CR2032 coin cells. In both cases, the

voltage profiles are similar, with a first discharge exhibiting two voltage pseudo-plateaus (at ca. 2.85 and ca. 0.6 V when using the *in-situ* cell) corresponding to the intercalation and conversion reactions, respectively. Also, in both electrochemical cells, reversible capacities surpassing the theoretical values for intercalation are observed.[18] The main variations between them lie, however, in the overpotential, which augmented from 0.5 V in the coin cell to ca. 1 V in the *in-situ* cell, and correspondingly in the lower reversible (oxidation) capacity delivered in the first cycle when using the *in-situ* cell for the same cut-off voltage. Although these relatively large polarizations are a feature commonly observed in conversion-type reactions, [6, 48] the larger hysteresis detected in the *in-situ* cell can result from the slightly inhomogeneous pressure applied to the system. This could be a consequence of the perforated body of this transmission cell (**Figure S4**b, c), necessary to allow the γ-rays to pass through it. This higher polarization and the difference noticed in the reversible capacity of the *in operando* cell can also be ascribed to the distinct electrode formulation, *i.e.*, to the larger mass loading of active material employed in the *in-situ* cell (39.2 mg, vs. the 8.5 mg in the coin cell). Nonetheless, the general reaction mechanism will be the same in both cells. It is also worth mentioning here that, the first cycle exhibits a large irreversible capacity regardless of the cell used. Despite the first-cycle irreversible capacity might jeopardize the practical application of Prussian blue-type materials, as generally occurs with other conversion anode materials, certain strategies, such a nanostructuring[49] or pre-lithiation[50] could help to alleviate this drawback.

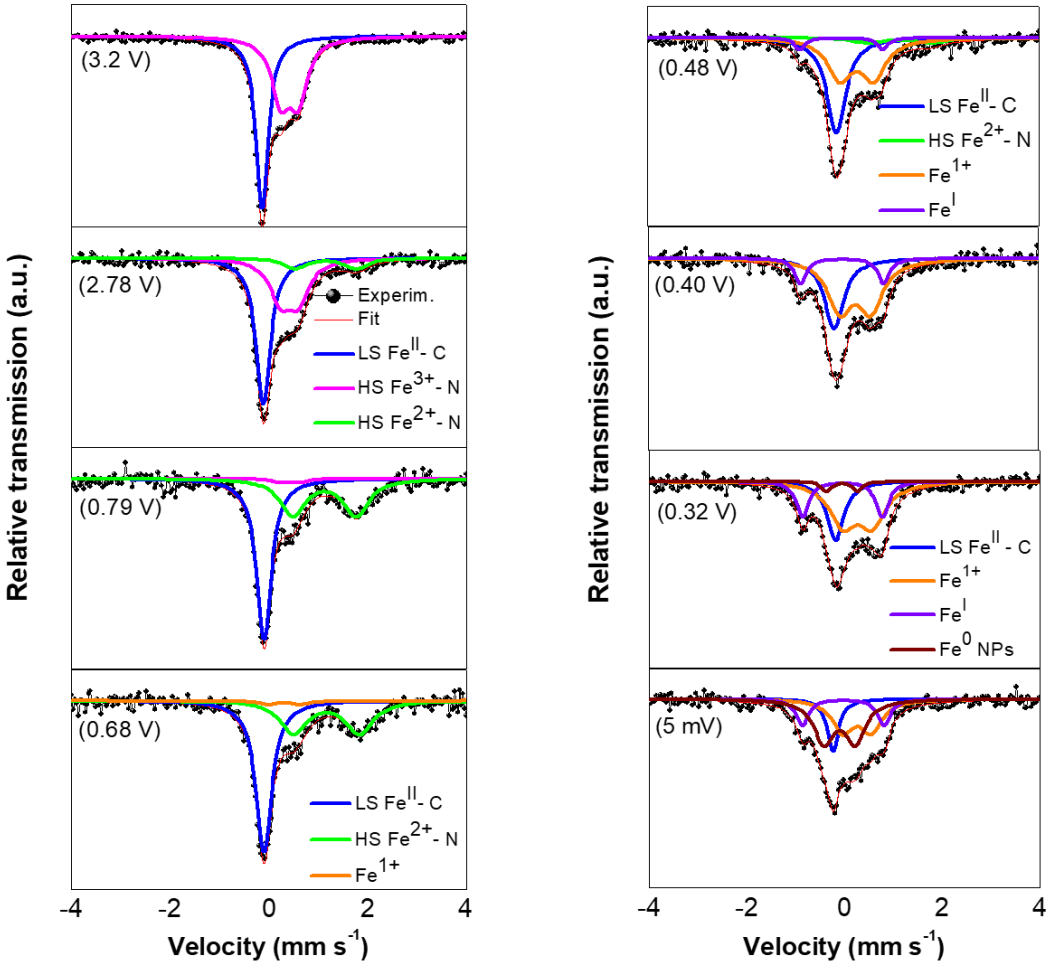

Figure 4. Mössbauer spectra obtained at different points of the first discharge of K-PB vs. Li^+/Li, when using the *in-situ* Mössbauer cell. Experimental (black dots) and fitting (red line) are shown along with the blue, pink, green, orange, purple and wine solid lines that represent the LS Fe^{II}-C, HS Fe^{3+}-N, HS Fe^{2+}-N, what seems Fe^{1+}, tentatively Fe^{I} and surface Fe^0 NPs spectral components, respectively.

The most relevant Mössbauer spectra collected using the *in-situ* Mössbauer cell along the first discharge of K-PB vs. metallic lithium are presented in **Figure 4**. For a better comparison, the total area of each spectrum has been normalized to one, i.e., to the Fe content. The spectrum of the

material at OCV (3.2 V) is very similar to that already shown in **Figure 2**b. It has two components: a singlet associated to LS Fe^{II} covalently coordinated to C (blue line) and a doublet assigned to HS Fe^{3+} ionically bonded to N (pink line). [39, 51] See **Table 2** for further details on the hyperfine parameters of the different Fe species present in the pristine material and those to which they evolve along the reduction process. At 2.78 V and below, a second doublet (green line) attributed to the formation of HS Fe^{2+}, resulting from the reduction of Fe^{3+}-N, can be distinguished. In the interval from 2.78 V to 0.79 V, the population of the new HS Fe^{2+} (green) increases whereas HS Fe^{3+} (pink) is consumed. Indeed, at 0.79 V, K-PB has completely evolved into Prussian White (LiK-PW, ideally $LiKFe^{2+}[Fe^{II}(CN)_6]$) and almost no trace of the initial Fe^{3+} is detected. As collected in **Table 2**, the parameters obtained from fitting LS Fe^{II} (blue) and HS Fe^{2+} (pink) are in agreement with those existing in the literature (LS Fe^{II} (δ = -0.05 mms^{-1}, Δ = 0 mms^{-1}) and HS Fe^{2+} (δ = 1.18 mms^{-1}, Δ = 1.58 mms^{-1})) for the K-PW (ideally $K_2Fe^{2+}[Fe^{II}(CN)_6]$) phase. [52] From 0.68 V downwards, a new doublet component appears (orange line). Considering the evolution of this type of iron along the electrochemical process – both discharge and charge (as we will see later) - and contrasting its isomer shift and quadrupole splitting values (**Table 2**), 0.27 and 0.66 mms^{-1}, with the hyperfine parameters reported for Fe^{+} in some organometallic species (**Table S1**), we presumably assign it to the unusual Fe^{1+}. Moreover, the proportion of this Fe^{1+} (orange) augments at the expense of the depletion of HS Fe^{2+} (plotted in green), and at 0.48 V there is almost no HS Fe^{2+} left. This implies that all the ionically bonded HS Fe^{2+}-N (green) is first reduced to Fe^{1+} (orange) while the LS Fe^{II}-C in $[Fe(CN)_6]^{4-}$ (blue) remains practically unaltered. Considering that Fe^{3+} has a HS d^5 configuration and Fe^{II} a LS d^6 configuration, and that CN^- is a high-field ligand that would favour LS configurations complexes, it is logical that HS Fe^{3+} was more prone to react in the first place. Between HS Fe^{2+} and LS Fe^{II} (both d^6 configuration), accordingly t_{2g}^4

e_g^2 and t_{2g}^6, the higher resistance to reduction of the latter is again due to its higher stability. At this point of discharge (0.48 V), an additional incipient doublet evolves (in purple). The formation of this new type of Fe is subject to the consumption of LS Fe^{II}, which was almost intact until then. The parameters of our new doublet (violet) do not match any previously reported signals. Although its isomer shift is -0.03 mms^{-1}, a value very close to that of body cubic centered (*bcc*) Fe, its very large quadrupole splitting (1.70 mms^{-1}) suggests it is another Fe species (**Table S1**) with structural environment different to that of *bcc* Fe or to the Fe^{1+} (orange) hailed from HS Fe^{2+}. We have tentatively assigned it to Fe^{I}. Yet, another Fe type (wine) appears at the very end of discharge, from 0.32 V down, by consumption of both Fe^{1+} (orange) and Fe^{I} (violet) species. The new species has hyperfine parameters (δ = -0.07 mms^{-1}, Δ = 0.69 mms^{-1}) in accordance with those reported for Fe^0 NPs from conversion reactions of spinels MFe_2O_4 (M = Co, Ni)[53] and iron carbodiimides FeNCN [54], and hence it is assigned to the formation of surface Fe^0 NPs. Although the Mössbauer signal of bulk Fe^0 is typically a sextuplet at low temperature, superparamagnetic iron NPs - as those typically generated in conversion reactions - only yield a singlet [55, 56] at room temperature. However, a doublet assigned to the formation of surface metallic Fe^0 NPs (see **Table S2**) is frequently found, prior to the appearance of the "bulk-superparamagnetic NPs" iron singlet.[57] The absence of the corresponding additional singlet in our experiment, characteristic of superparamagnetic Fe^0 NPs, can be explained by the *operando* nature of our experiment and the small particle size of the starting material (ca. 5 - 10 nm, as reported elsewhere [18]). For the record, a 2-weeks hold in the discharged state (0 V vs. Li^+/Li) was required to observe the singlet (superparamagnetic Fe^0) in another study with Sn_2Fe.[27] Additionally, the lack of SPM Fe^0 NPs can also be hinted from the appearance of the ^{19}F and ^6Li solid state Nuclear Magnetic Resonance

(ssNMR) spectra of a fully discharged electrode (**Figure S5**), which did not show any of the features associated to the presence of "bulk-superparamagnetic NPs".

Table 2. Hyperfine parameters δ, Δ, WID, % Fe and χ^2 extracted from the Mössbauer fitting for ^{57}Fe in K-PB vs. Li^+/Li along the first discharge curve (δ = isomer shift relative to *bcc* Fe, Δ = quadrupolar splitting, WID = width at half height, % Fe = atomic Fe %, χ^2 = chi square values or goodness of fitting). The values in parenthesis indicate the deviation with respect to the average value for each component, as the species slightly change within the reduction process.

Voltage (V)[a]	Assignment	**δ** (mms^{-1})	**Δ** (mms^{-1})	**WID** (mms^{-1})	**%Fe**	χ^2 [d]
0.79 V	HS Fe^{3+} (pink)	0.42(1)	0.36(1)	0.45(7)	2.3[c]	0.919
0.48 V	HS Fe^{2+} (green)	1.16(4)	1.30(5)	0.65(6)	2.7[c]	0.933
5 mV	LS Fe^{II} (blue)	- 0.22(3)	0	0.33(8)	13.6	0.909
	Fe^{1+} (orange)	0.27(2)	0.66(6)	0.62(4)	30.8	
	Fe^{I} (violet)	-0.03(2)	1.70(3)	0.26(2)	15.3	
	[b] Fe^0 (wine)	-0.07(3)	0.69(5)	0.35(12)	40.2	

[a] voltage down to which each type of iron is stable (vs. Li^+/Li), [b] surface Fe^0 NPs, [c] please note that the *in situ* Mössbauer spectra were collected each 15 min, hence, the exact voltage at which the % Fe would be 0% for a particular iron species cannot be extrapolated; however, we can assume that 0% of Fe will be achieved at potentials slightly below those provided in this table, [d] χ^2 values correspond to the goodness of fitting all the components present in a spectrum at a particular voltage.

For further clarification, **Figure 5** graphically summarizes the conclusions extracted from the ^{57}Fe-Mössbauer data discussion concerning the first discharge of K-PB vs. Li^+/Li, compiling the evolution of the iron species that exists in the pristine electrode and those presumably generated along the reduction process.

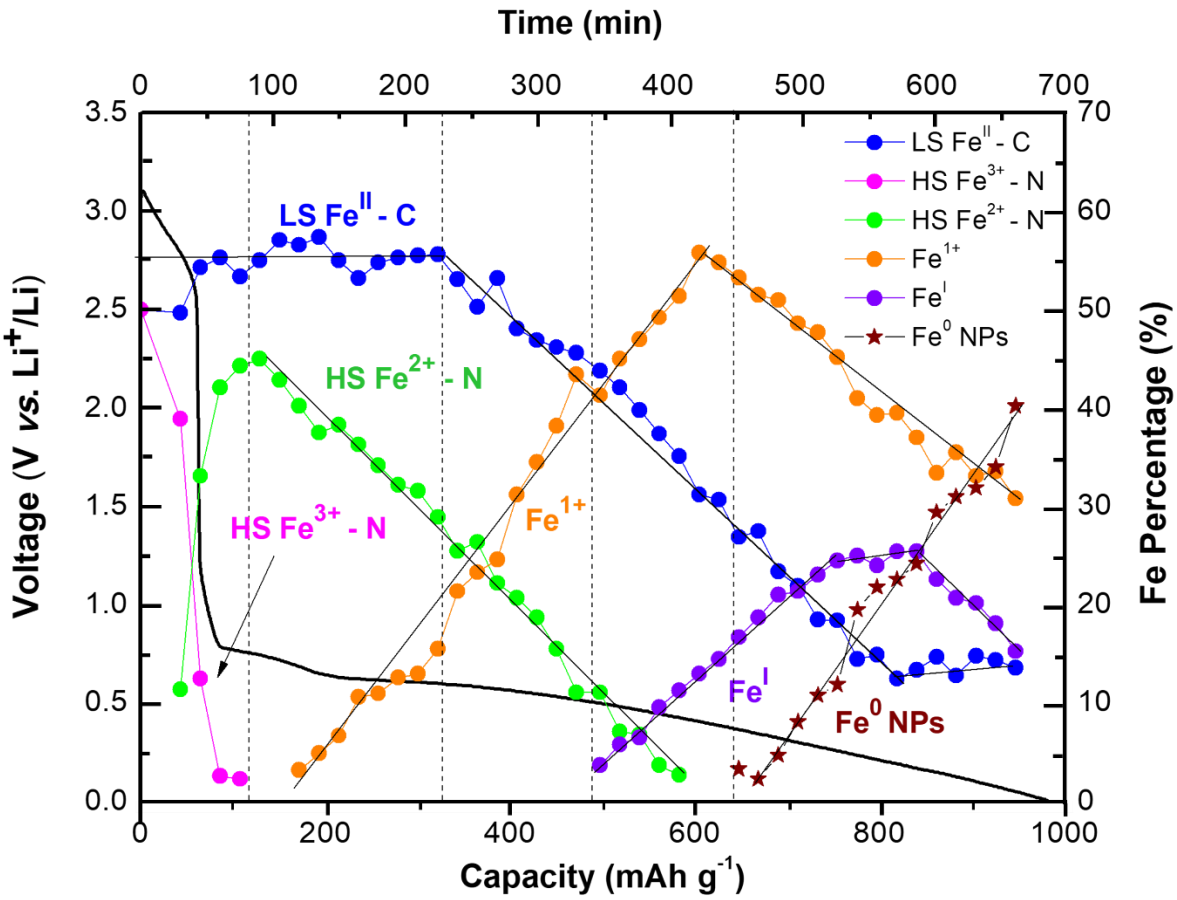

Figure 5. Evolution of the different iron spectral components observed along the first discharge process of K-PB vs. Li^+/Li. The pink, blue, green, orange and purple circles represent, respectively, HS Fe^{3+}-N, LS Fe^{II}-C, HS Fe^{2+}-N, Fe^{1+} and tentatively Fe^{I}; and the wine stars are assigned to surface Fe^0 NPs.

As it can be clearly observed above 800 mA h g^{-1}, whereas the population of LS Fe^{II} (blue) remains constant, the rise in the percentage (of up to 40%) of surface Fe^0 NPs (wine) is so sharp that cannot be fully explained as a result of the 25% decrease of Fe^{1+}-N (orange), but it is also a consequence of the 13% reduction observed in the iron species plotted in violet. The fact that the population of surface Fe^0 (wine) increases at the expense of Fe^{1+} and Fe^{I} species (orange and purple) while continue reducing the voltage, undoubtedly reinforces the hypothesis that these iron species are

both in oxidation state +1. Interestingly, not all LS Fe^{II} (blue) is reduced at the end of the discharge, with ca. 20% of it remaining as $[Fe^{II}(CN)_6]^{4-}$. In consequence, a minimal fraction of the -Fe-C≡N- structure is preserved, which we believe that positively affects the reversibility of the reaction. Likewise, the fact that the Fe^0 formed are just surface NPs (wine) would also help in its oxidation process. In summary, we can compile the evolution of both Fe oxidation states during the 1st discharge as follows (see Equation (**5**)):

$$\text{HS } Fe^{3+}\text{-N} + \text{LS } Fe^{II}\text{-C} \xrightarrow[+\,e^-]{+\,Li^+} \text{HS } Fe^{2+}\text{-N} + \text{LS } Fe^{II}\text{-C} \xrightarrow[+\,e^-]{+\,Li^+} Fe^{1+}\text{-N} + \text{LS } Fe^{II}\text{-C} \xrightarrow[+\,xe^-]{+\,xLi^+}$$

$$Fe^{1+}\text{-N} + x\ Fe^{I}\text{-C} + (1\text{-}x)\ \text{LS } Fe^{II}\text{-C} \xrightarrow[+(y+z)e^-]{+(y+z)Li^+} (y+z)\ Fe^0 + (1\text{-}y)\ Fe^{1+}\text{-N} + (x\text{-}z)Fe^{I}\text{-C} \qquad (\mathbf{5})$$

$$+ (1\text{-}x\text{-}z)\ \text{LS } Fe^{II}\text{-C}$$

During the first stage of charge (see **Figure 6** and **Figure S6)**, from the totally discharged state (5 mV) to 0.77 V, the Fe^{1+} population (orange) seems to augment slightly at the expense of the surface Fe^0 NPs (wine) consumption, while the Fe^I (violet) and the LS Fe^{II} (blue) populations stay almost changeless. Then, in the 0.77 – 1.14 V vs. Li^+/Li range, a considerable increase of about 11% of the Fe^{1+} population (orange) is apparently observed as a result of a decline of ca. 14% in surface Fe^0 species (wine), accompanied by a slight 5% increment of Fe^I (violet) and a decrease of approx. 3% in LS Fe^{II} (blue). Please bear in mind that although 3-5% variation may not be statistically significant, we aim to provide trends in the Fe % evolution. Despite the rise of reduced species and the decrease of oxidized species are not expected during the oxidation process, this fact could be explained by an "electrochemically stimulated" chemical comproportionation of Fe^{II} and Fe^0 to yield Fe^I in addition to the electrochemical $Fe^0 \rightarrow Fe^+$ direct oxidation, what also supports the

theory that the violet component is Fe^{I} (instead of Fe^{0}). Above 1.14 V, the amount of Fe^{1+} (orange) continues growing while depleting Fe^{0} (wine). A mild increment of the percentage of LS Fe^{II} (blue) due to the slight descent of the corresponding Fe^{I} (violet) is also detected. The growth in Fe^{I} population (violet), followed by its fall at intermediate points of the oxidation curve (between 1.14 and 1.6 V), may manifest some type of competitiveness between the LS Fe^{II} (blue) and Fe^{1+} (orange). Although the isomer shift and quadrupolar values may suggest that both Fe^{1+} and Fe^{I} formed may be LS, the spin state (either HS or LS) of these species could not be determined, given the limited information (**Table S2**) available regarding Fe(I) complexes characterized by ^{57}Fe-Mössbauer in the literature. If these species were stable, further assignment of the spin state of Fe(I) (S = 3/2 or 1/2) could be obtained from magnetic susceptibility measurements[58]. Nonetheless, it is quite unlikely that Fe^{1+} and Fe^{I} remain invariant in that unusual oxidation state once we stop applying a continuous voltage and disassemble the *in operando* cell (in a glove box), to prepare the sample for such magnetic measurements. We firmly believe that we were able to identify the generation of Fe(I) species thanks to the utilization of an *in operando* cell. Otherwise, only metastable species, such as Fe(II) and Fe(0), would have been detected, as proven when other *ex-situ* experiments, such as XAS, are conducted.

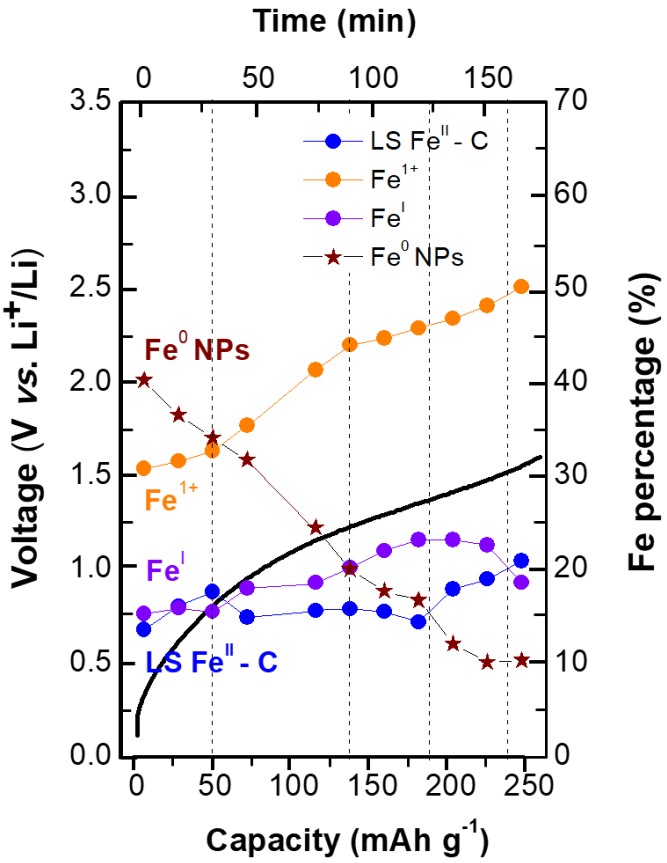

Figure 6. Evolution of the different iron spectral components observed along the first charge of K-PB vs. Li^+/Li. The blue, orange and purple circles represent, respectively, the LS Fe^{II}-C, Fe^{1+} and tentatively Fe^{I}; and the wine starts are assigned to surface Fe^0 NPs.

In brief, the charge reaction is dominated by the oxidation of Fe^0 NPs to Fe^{1+}, so there is no reason to think that limiting the lower cut-off voltage to avoid the formation of surface Fe^0 NPs would result in any improvement of performance. The percentage of Fe^0 decreases from 40% to 10%, contrasting to the increase in the population of Fe^{1+} from 30% to 50%. Additionally, in general terms, a rise of both Fe^{I} (violet) and LS Fe^{II} (blue) populations also occurs (from ca. 15 to ca. 20%, in both cases) before any oxidation of Fe^{1+} to HS Fe^{2+} could be observed. There is, indeed, an asymmetry in the sequence of reduction and oxidation reactions at the two Fe sites, since the more

ionic N-Fe is prone to react earlier both in reduction and oxidation. However, the reversibility of the cycling process is undeniable, as already proven by the electrochemistry (**Figure 1**b) and the XAS spectra (**Figure 3**). The hyperfine parameters of the different Fe components at each stage and their variation along the oxidation process are summarized in **Table S3**. According to the changes in the Fe oxidation state discussed to take place during charge (Figure 6), 65 mAh g^{-1} would be due to oxidation of Fe^0 to $Fe^{1+/I}$ and to LS Fe^{II}. However, experimentally 250 mAh g^{-1} are observed. The remaining 185 mAh g^{-1} must be due to additional reversible processes, such as to Li^+ insertion into the 20 *wt.%* conducting carbon at very low voltages[59] and other processes reported to occur in conversion reactions, e.g., LiOH formation and subsequent generation of LiH and Li_2O in OH-containing systems or materials,[60] as it is K-PB. Actually, LiOH had already been detected at the end of the K-PB discharge,[18] as stated in the introduction. Although the contribution of the Fe redox processes to the reversible capacity may seem low, this is most likely due to the large voltage hysteresis seen in the measurements conducted with the *in-situ* Mossbauer cell. However, its contribution is larger in Swagelok and coin-type cells (as **Figure S4** corroborates), reaching an oxidation capacity of 400 mAh g^{-1} in the same voltage range and C-rate, a value above the maximum 350 mAh g^{-1} due to $Fe^0/Fe^{1+/I}/Fe^{2+/II}$ redox pairs.

The formation of Fe^0 NPs is unequivocally confirmed by *ex-situ* XAS analyses and *in-situ* ^{57}Fe-Mössbauer experiments. Although the percentage of Fe^0 estimated in the totally discharged state by the two techniques here used differs slightly, from approx. 58% according to XAS to 40% based on ^{57}Fe-Mössbauer analysis, it is important to bear in mind that the former measurements were conducted *ex-situ*, hence, giving some time for the present metastable Fe^{1+} species to evolve towards equilibrium and increase the population of those more stable Fe^{2+} and Fe^0 species, while the Mössbauer experiments were done *in operando* (out of thermodynamic equilibrium). It seems

then that the Fe^{+} species, if not thermodynamically stable (which remains to be proven), are highly favored during electrochemical cycling, as its formation occurs even from Fe^{II} during oxidation. The stability of these Fe^{+} could be key to explaining the good reversibility with lower electrochemical potential in this Prussian Blue system with respect to conversion reactions of other Fe species. Indeed, this K-PB shows about 0.5 V of hysteresis at ~ 9 mAh g^{-1}, while 0.7 V are seen in iron oxofluorides,[61] 0.9 V in iron oxides[25] and 1.2 V in iron fluorides[26]. Although Mossbauer studies have not been performed for most of these systems, a detailed *in situ* Mössbauer investigation on Fe_2O_3 [62] did not show any additional signal in between the disappearance of Fe^{2+} and formation of Fe^{0} nanoparticles.

To summarize, in addition to confirming the conversion reaction mechanism for K-PB at low voltages in LIBs through XAS data, Mössbauer results show the surprising formation of two intermediate Fe^{I} and Fe^{1+} species during lithiation, prior to the full reduction to Fe^{0} NPs. To the best of our knowledge, this is one of the few times that the formation of species with metals in oxidation state +1 are speculated for anode materials in the battery field, [16, 17, 22] the first time for iron and the first time that it is supported by experimental evidences (^{57}Fe-Mössbauer spectra). These species, Fe^{0} NPs, Fe^{1+} and Fe^{I}, are also involved and are crucial in the charge process, which seems to be facilitated with respect to conversion reactions where direct $Fe^{2+} \leftrightarrows Fe^{0}$ reaction with higher overpotential associated takes place.

CONCLUSIONS

The conversion reaction that K-PB experiences when cycled in the low voltage region (1.6 - 0.005 V vs. Li^{+}/Li) as anode material in LIBs has been proved within this study, through *ex-situ* XAS

and *in operando* Mössbauer experiments. *Ex-situ* XAS measurements in the XANES region reflect the evolution of Fe^{3+}-N and Fe^{II}-C present in the pristine material to Fe^0 NPs upon discharge, reaching a population of the latter greater than 58% at the end of discharge. The EXAFS region suggests the rupture of some of the Fe-C≡N-Fe bond after the first discharge. Besides, *in-situ* Mössbauer data collected *in operando* while electrochemically cycling K-PB allowed to detect two intermediate Fe species, Fe^{1+} and Fe^{I}, and elucidate a sequential mechanism for the conversion reaction of each of the two Fe species. Along the discharge process, HS Fe^{3+}-N gets first reduced to HS Fe^{2+} linked to N, forming Prussian White, as expected. Next, the Prussian White structural framework evolves and undergoes an initial reduction step for the conversion reaction (HS Fe^{2+}-N → Fe^{1+}-N), while the $[Fe^{II}(CN)_6]^{4-}$ units are preserved. Before all HS Fe^{2+}-N is converted into Fe^{1+}-N, LS Fe^{II}-C starts reacting forming what we have assigned to Fe^{I}-C. Once all the Fe^{2+} has been transformed into Fe^{1+}, a new species ascribed to surface Fe^0 NPs is formed at the expense of both Fe^{1+} and Fe^{I}, confirming the expected conversion reaction.

As for the oxidation process (charge), the population of Fe^{1+}, Fe^{I} and LS Fe^{2+}-C augments whereas that of Fe^0 decreases. As the totality of LS Fe^{2+}-C is not consumed in the first reduction and a little fraction remains available, this and the formation of stable Fe^{+} species help to decrease the overpotential - compared to the conversion reactions of other Fe-based compounds - and guarantees the reversibility of the redox reaction.

ASSOCIATED CONTENT

See **Supporting Information**.

- TGA analysis, SEM images and XPS spectra of the pristine material; overlapped representation of the Fe K-edge XANES spectra collected *ex-situ* for K-PB electrodes cycled vs. Li^+/Li up to/down to the same potential; XAS spectra at the Fe K-edge in the EXAFS region along the first (dis)charge and second discharge of K-PB vs. Li^+/Li; comparative voltage profile of K-PB electrochemically cycled in a coin cell and the *in operando* cell, accompanied with a detailed description of the *in operando* cell; table collecting the hyperfine Mössbauer parameters of some Fe^+-containing complexes reported in the literature; table gathering some available information about hyperfine Mössbauer parameters for Fe^0-containing materials, and how they contrast with the values obtained in this work; ss ^{19}F- and ^6Li-NMR spectra of K-PB at the end of the first discharge, along with a brief description of the results; selected Mössbauer spectra obtained at different points of the first charge of K-PB vs. Li^+/Li; and hyperfine parameters extracted from the Mössbuer fitting for LiK-PB along the first charge.

AUTHOR INFORMATION

Corresponding Author

Present Adresses

* María José Piernas-Muñoz. Inorganic Chemistry Department, University of Murcia, C/Campus Universitario 5, 30100 Murcia, SPAIN. mjpiernas@um.es

Elizabeth Castillo-Martínez. Department of Chemistry, Complutense University of Madrid, Plaza de las Ciencias 2, 28040 Madrid, SPAIN. ecastill@ucm.es

Author Contributions

The manuscript was written through contributions of all authors. All authors have given approval to the final version of the manuscript.

Notes

The authors declare no conflict of interest.

ACKNOWLEDGMENTS

This work was financially supported by the Basque Government (Etortek 2014) and the Ministry of Economy and Competitivity of the Spanish Government (Project LINABATT ENE2013-44330-R). Mª José Piernas Muñoz thanks the Basque Government for the predoctoral grant "Nuevas Becas y renovaciones para el Programa Predoctoral de Formación del Personal Investigador" (PRE_2013_1_790). The authors of this work would like to thank Oleksandr Bondarchuk for his help on measuring the XPS spectrum.

This research used resources of the Advanced Photon Source (APS), an U.S. Department of Energy (DOE) Office of Science User Facility operated for the DOE Office of Science by Argonne National Laboratory under Contract No. DE-AC02-06CH11357. Fister and Jonhson were supported by the Center for Electrochemical Energy Science, an Energy Frontier Research Center funded by the U.S. Department of Energy, Office of Science, Basic Energy Sciences.

REFERENCES

[1] Luo, X.; Wang, J.; Dooner, M.; Clarke J. Overview of current development in electrical energy storage technologies and application in power system operation. *Applied Energy* **2015**, 137, 511-536.

[2] Goodenough, J. B.; Park, K-S. The Li-Ion Rechargeable Battery: A Perspective. *J. Am. Chem. Soc*. **2013**, *135 (4)*, 1167-1176.

[3] Armand, M.; Tarascon, J-M. Building better batteries. *Nature* **2008**, *451*, 652-657.

[4] Linden, D.; Reddy, T. B. *Handbook of Batteries*, 3rd edition; McGraw-Hill: New York, 2002.

[5] Dunn, B.; Kamath, H.; Tarascon, J-M. Electrical Energy Storage for the Grid: A Battery of Choices. *Science* **2011**, *334*, 928.

[6] Nitta, N.; Wu, F; Lee, J. T.; Yushin, G. Li-ion battery materials: present and future perspectives. *Materials Today* **2015**, *18 (5)*, 252-264.

[7] Ohzuku, T.; Owakoshi, Y.; Sawai. K. Formation of Lithium-Graphite Intercalation Compounds in Nonaqueous Electrolytes and Their Applications as Negative Electrode for a Lithium Ion (Shuttlecok) Cell. *J. Electrochem. Soc.* **1993**, *140 (9)*, 2490-2498.

[8] Cabana, J.; Monconduit, L.; Larcher, D.; Palacín, M. R. Beyond Intercalation-Based Li-ion Batteries: The State of the Art and Challenges of Electrode Materials Reacting Through Conversion Reactions. *Adv. Mater.* **2010**, *35 (22)*, E170-E192.

[9] Hua, X.; Allan, P. K.; Gong, C.; Chater, P. A.; Schmidt, E. M.; Geddes, H. S.; Robertson, A. W.; Bruce, P. G.; Goodwin, A. L. Non-equilibrium metal oxides via reconversion chemistry in lithium-ion batteries. *Nature Comm*. **2021**, *12*, 561.

[10] Piernas-Muñoz, M. J.; Castillo-Martínez, E. *Prussian Blue Based Batteries*; Springer Briefs in Applied Science and Technology, Springer Nature: Cham, 2018.

[11] Brown, D.B.; Shriver, D.F. Structure and solid-state reactions of Prussian blue analogs containing chromium, manganese, iron and cobalt. *Inorg. Chem.* **1969**, *8*, 37.

[12] Wessells, C. D.; Huggins, R. A.; Cui Y. Copper hexacyanoferrate battery electrodes with long cycle life and high power. *Nat. Commun.* **2011**, *2*, 550.

[13] Keggin, J. F.; Miles, F. D. Structures and Formulae of the Prussian Blues and Related Compounds. *Nature* **1936**, 577.

[14] Lu, Y.; Wang, L.; Cheng, J.; Goodenough, J. B. Prussian blue: a new framework of electrode materials for sodium batteries. *Chem. Commun.* **2012**, *48*, 6544-6546.

[15] Shokouhimehr, M.; Yu, S-H.; Lee, D-C.; Ling, D.; Hyeon, T.; Sung, Y-E. Metal Hexacyanoferrate Nanoparticles as Electrode Materials for Lithium Ion Batteries. *Nanosci. Nanotechnol. Lett.* **2013**, *5*, 7.

[16] Nie, P.; Shen, L.; Luo, H.; Ding, B.; Xu, G.; Wang, J.; Zhang, X. Prussian blue analogues: a new class of anode materials for lithium-ion batteries. *J. Mater. Chem. A* **2014**, *2*, 5852.

[17] Xiong, P.; Zeng, G.; Zeng, L.; Wei, M. Prussian Blue analogues $Mn[Fe(CN)_6]_{0.6667}\cdot nH_2O$ cubes as an anode material for lithium-ion batteries. *J. Dalton Trans.* **2015**, *44* (38), 16746 – 16751.

[18] Piernas-Muñoz, M. J.; Castillo-Martínez, E.; Roddatis, V.; Armand, M.; Rojo, T. $K_{1-x}Fe_{2+x/3}(CN)_6\cdot yH_2O$, Prussian Blue as a displacement anode for lithium-ion batteries. *J. Power Sources* **2014**, *271*, 489-496.

[19] Goriparti, S.; Miele, E.; De Angelis, F.; Di Fabrizio, E.; Proietti Zaccaria, R.; Capiglia, C. Review on recent progress of nanostructured anode materials for Li-ion batteries. *J. Power Sources* **2014**, *257*, 421-443.

[20] Sun, X.; Ji, X-Y.; Zhou, Y-T.; Shao, Y.; Zang, Y.; Wen, Z-Y.; Chen, C-H. A new gridding cyanoferrate anode material for lithium and sodium ion batteries: $Ti_{0.75}Fe_{0.25}[Fe(CN)_6]_{0.96}\cdot 1.9H_2O$ with excellent electrochemical properties. *J. Power Sources* **2016**, *314*, 35-38.

[21] Shibata, T.; Takachi, M.; Moritomo, Y. Low Voltage Charge/Discharge Behaviour of Manganese Hexacyanoferrate. *Batteries* **2017**, *3*, 7.

[22] Zhou, F-C.; Sun, Y-H.; Li, J-Q.; Nan, J-M. $K_{1-x}Fe_{1+x/2}[Fe(CN)_6]\cdot yH_2O$ Prussian blue analogues as anode material for lithium-ion batteries. *Appl. Surf. Sci.* **2018**, *444*, 650-660.

[23] He, X.; Tian, L.; Qiao, M.; Zhang, J.; Geng, W.; Zhang, Q. A novel highly crystalline $Fe_4[Fe(CN)_6]_3$ concave cube anode material for Li-ion batteries with high capacity and long life. *J. Mater. Chem. A* **2019**, *7*, 11478.

[24] Lee, H-W.; Wang, R. Y.; Pasta, M.; Lee, S. W.; Liu, N.; Cui. Y. Manganese hexacyanomanganate open framework as a high-capacity positive electrode material for sodium-ion batteries. *Nat. Comun*. **2014**, *5*, 5280.

[25] Hua, X.; Allan, P. K.; Geddes, H. S.; Castillo-Martínez, E.; Dean, T. S.; Minelli, A.; Bruce, P. G.; Goodwin, A. L. Lithiation phase behaviors of metal oxide anodes and extra capacities. *Cell Reports Physical Science* **2021**, *2*, 100543.

[26] Hua, X.; Eggeman, A. S.; Castillo-Martínez, E.; Robert, R.; Geddes, H. S.; Lu, Z.; Pickard, C. J.; Meng, W.; Wiaderek, K. M.; Pereira, N.; Amatucci, G. G.; Midgley, P. A.; Chapman, K. W.; Steiner, U.; Goodwin, A. L.; Grey, Clare P. Revisiting metal fluorides as lithium-ion battery cathodes. *Nature Materials* **2021**, *20*, 841-850.

[27] Mao, O.; Dunlap, R. A.; Courtney, J. A.; Dahn, J. R. In situ Mössbauer Effect Studies of the Electrochemical Reaction of Lithium with Mechanically Alloyed Sn_2Fe. *J. Electrochem. Soc.* **1998**, *145* (12), 4195-4202.

[28] Dunlap, R. A.; Mao, O. Application of in situ Mössbauer effect methods for the study of electrochemical reactions in lithium-ion battery electrode material. *Phys. Rev. B* **1999**, *59* (5), 3494 – 3500.

[29] Ionica-Bousquet, C. M.; Lippens, P. E.; Aldon, L.; Olivier-Fourcade, J.; Jumas, J. C. In situ ^{119}Sn Mössbauer Effect Study of Li-$CoSn_2$ Electrochemical System. *Chem. Mater*. **2006**, *18*, 6442-6447.

[30] Aldon, L.; Perea, A.; Womes, M.; Ionica-Bousquet, C. M.; Jumas J.-C. Determination of the Lam-Mössbauer factors of $LiFePO_4$ and $FePO_4$ for electrochemical in situ and operando measurements in Li-ion batteries. *J. Solid State Chem.* **2010**, *183*, 218-222.

[31] Sougrati, M. T.; Fullenwarth, J.; Debenedetti, A.; Fraisse, B.; Jumas, J. C.; Monconduit, L. TiSnSb a new efficient negative electrode for Li-ion batteries: mechanism investigations by operando-XRD and Mössbauer techniques. *J. Mater. Chem.* **2011**, *21*, 10069.

[32] Harks, P. P. R. M. L.; Mulder, F. M.; Notten, P. H. L. In situ methods for Li-ion battery research: A review of recent developments. *J. Power Sources* **2015**, *288*, 92-105.

[33] Penner-Hahn, J. E. *X-ray Absorption Spectroscopy*; In eLS, John Wiley & Sons, Ltd (Ed.): **2005**.

[34] B. Ravel, M. Newville. ATHENA, ARTHEMIS, HEPHAESTUS: data analysis for X-ray absorption spectroscopy using IFEFFIT. *J. Synchrotron Radiat.* **2005**, *12*, 537–541.

[35] N. N. Greenwood, *Mössbauer Spectroscopy*, Springer, London, **1971**. Chapter 1 and 3 (pages 1-16, 46-79).

[36] R. A. Brand, Nörmos Mössbauer Fitting Program, Univ. Duisburg, 2002, http://physics-astronomy-manuals.wwu.edu/Wissel%20NORMOS%2090%20Manual.pdf

[37] U. Groß, S. Rüdiger, A. R. Grimmer, E. Kemnitz. *J. Fluorine Chem*. **2002**, *115*, 193−199.

[38] Roberto Bueno, P.; Furlan Ferreira, F.; Giménez-Romero, D.; Oliveira Setti, G.; Censi Faria, R.; Gabrielle, C.; Perrot, H.; García-Jareño, J. J.; Vicente, F. Synchrotron Structural Characterization of Electrochemically Synthesized Hexacyanoferrates Containing K^+: A Revisited Analysis of Electrochemical Redox. *J. Phys. Chem. C* **2008**, *112* (34), 13264-13277.

[39] Samain, L.; Granjean, F.; Long, G. J.; Martinetto, P.; Bordet, P.; Strivay, D. Relationship between the Synthesis of Prussian Blue Pigments, Their Color, Physical Properties, and Their Behaviour in Paint Layers. *J. Phys. Chem. C* **2013**, *117* (19), 9693 (2013).

[40] Datta M., Datta A. In situ FTIR and XPS studies of the hexacyanoferrate redox system. *J. Phys. Chem.* **1990**, *94*, 8203-8207.

[41] Wu Q., Wu G., Wang L., Hu W., Wu H. Facile synthesis and optical properties of Prussian Blue microcubes and hollow Fe_2O_3 microboxes. *Sci. in Semicond. Process* **2015**, *30*, 476-481.

[42] Desimoni E., Brunetti B. X-ray Photoelectron Spectroscopic Characterization of Chemically Modified Electrodes Used as Chemical Sensors and Biosensors: A review. *Chemosensors* **2015**, *3*, 70-117.

[43] Chadwick A. V.; Savin S. L. P.; Fiddy S., Alcántara R., Fernández Lisbona D.; Lavela P.; Ortiz G. F.; Tirado J. L. Formation and Oxidatio of Nanosized Metal Particles by Electrochemical Reaction of Li and Na with NiCo2O4: X-ray Absorption Spectroscopic Study. *J. Phys. Chem*. **2007**, *111*, 4636-4642.

[44] Pohl, A.; Faraz, M.; Schrörder, A.; Baunach, M., Schabel, W.; Guda, A.; Shapovalov, V.; Soldatov, A.; Chakravadhanula, V. S. K.; Kübel, C.; Witte, R.; Hann, H.; Diemant, T.; Behm, R. J.; Emerich, H.; Fichtner, M. Developments of water based process for stable conversion cathodes on the basis of Fe_3F. *Journal of Power Sources* **2016**, *313*, 213-222.

[45] Buser, H.J.; Shwarzenbach, D.; Petter, W.; Ludi, A. The crystal structure of Prussian Blue: $Fe_4[Fe(CN)_6]_3.xH_2O$. *Inorg. Chem*. **1997**, *16* (11), 2704–2710.

[46] Wardecki, D.; Ojwang, D. O.; Grins, J.; Svensson, G.. Neutron Diffraction and EXAFS Studies of $K_{2x/3}Cu[Fe(CN)_6]_{2/3}\cdot nH_2O$. *Cryst. Growth Des.* **2017**, *17* (3), 1285-1292.

[47] Glatzel, P. ; Jacquamet, L. ; Bergann, U. ; de Groot, F. M. F. ; Cramer, S. P. Selective EXAFS in Mixed-Valence Compunds Using High-Resolution Fluorescence Detection: A Study of Iron Prussian Blue. *Inorg. Chem*. **2002**, *41*, 3121-3127.

[48] Yu, S-H; Lee, S. H.; Lee, D. J.; Sung, Y-E.; Hyeon, T. Conversion reaction-based oxide nanomaterials for Lithium Ion Battery Anodes. *Small* **2016**, *12* (16), 2146-2172.

[49] López, M. C.; Ortiz, G. F.; Lavela, P.; Alcántara, R.; Tirado, J. L. Improved Energy Storage Solution Base don Hybrid Oxide Materials. *ACS Sustainable Chem. Eng.* **2013**, *1*, 46-56.

[50] Zhan, R.; Wang, X; Chen, Z., She, Z. W.; Wang, L.; Sun, Y. Promises and Challenges of the Practical Implementation of Prelithiation in Lithium-Ion Batteries. *Adv. Energy Mater.* **2021**, *11 (35)*, 2170138.

[51] Duncan, J. F.; Wigley, P. W. R. Electronic Structure of the Iron Atoms in Complex Iron Cyanides. *J. Chem. Soc*. **1963**, *0*, 1120-1125.

[52] Hu, M. ; Jiang, J. S. Facile synthesis of air-stable Prussian White Microcubes via hydrothermal method. *Mat. Res. Bull.* **2011**, *46*, 702–707.

[53] Tirado, J. L.; Lavela, P.; Pérez Vicente, C.; León, B.; Vidal-Abarca, C. Unfolding the role of iron in Li-ion conversión electrode materials by ^{57}Fe Mössbauer spectroscopy. *Hyperfine Interact.* **2012**, *207*, 53-59.

[54] Sougrati, M. T. ; Darwiche, A. ; Liu, X. ; Mahmoud, A. ; Hermann, R. P. ; Jouen, S.; Monconduit, L.; Dronskowski, R.; Stievano, L. Transition-Metal Carbodiimides as Molecular Negative Electrode Materials for Lithium- and Sodium-Ion Batteries with Excellent Cycling Properties. *Angew. Chem. Intern. Ed.* **2016**, *55*, 5090-5095.

[55] Ferrandon, M.; Kopf, A. J.; Myers, D. J.; Artyushkova, K.; Kramm, U.; Bogdanoff, P.; Wu, G.; Johnston, C. M.; Zelenay, P. Multitechnique Characterization of a Polyaniline-Iron-Carbon Oxygen Reduction Catalyst. *J. Phys. Chem. C* **2012**, *116* (30), 16001–16013.

[56] Varnell, J. A.; Tse, E. C. M.; Schulz, C. E.; Fister, T. T.; Hassch, R. T.; Timoshenko, J.; Frenkel, A. I.; Gewirth, A. A. Identification of carbon-encapsulated iron nanoparticles as active species in non-precious metal oxygen reduction catalysts. *Nat. Commun.* **2016**, *7*, 12582.

[57] Obrovac, M. N.; Dunlap, R. A.; Sanderson, R. J.; Dahn, J. R. The Electrochemical Displacement Reaction of Lithium with Metal Oxides. *J. Electrochem. Soc.* **2001**, 148 (6), A576-588.

[58] Samuel P. P.; Mondal, K. C.; Sk, N. A.; Hebert W. R.; Neufield, R.; Dietmar, S.; Demeshko, S.; Meyer, F.; Ungur, L., Chibotaru, L. F.; Christian, J.; Ramachandran, V.; van Tol, J.; Dalal, N. S. Electronic Structure and Slow Magnetic Relaxation of Low Coordinate Cyclic Alkyl(amino)Carbene Stabilized Iron(I) Complexes. *J. Am. Chem. Soc.* **2014**, *136*, 11964-11971.

[59] See, K. A.; Lumley M. A.; Stucky G. D.; Grey C. P., Seshadri R. Reversible Capacity of Conductive Carbon Additives at Low Potentials: Caveats for Testing Alternative Anode Materials for Li-Ion Batteries. *J. Electrochem. Soc.* 2017, **164,** A327.

[60] Hu, Y-Y.; Liu, Z.; Nam, K-W.; Borkiewicz, O. J.; Cheng, J.; Hua, X.; Dunstan, M. T.; Yu, X.; Wiaderek, K. M.; Du, L-S.; Chapman, K. W.; Chupas, P. J.; Yang, X-Q.; Grey, C. P. Origin of additional capacities in metal oxide lithium-ion battery electrodes. *Nat. Mater.* **2013**, *12*, 1130–1136.

[61] Wiaderek, K. M.; Borkiewicz, O. J.; Castillo–Martínez, E.; Robert, R.; Pereira, N.; Amatucci, G. G.; Grey, C. P.; Chupas, P. J.; Chapman, K. W. Comprehensive Insights into the Structural and Chemical Changes in Mixed-Anion FeOF Electrodes by Using Operando PDF and NMR Spectroscopy. *J. Am. Chem. Soc.* **2013**, *135*, 4070-4078.

[62] Larcher, D.; Bonnin, D.; Cortes, R.; Rivals, I.; Personnaz, L.; Tarascon, J.-M. Combined XRD, EXAFS, and Mössbauer Studies of the Reduction by Lithium of α-Fe_2O_3 with Various Particle Sizes. *J. Electrochem. Soc.* **2003**, *150* (12), A1643-A1650.

TABLE OF CONTENTS

Prussian blue undergoes a conversion reaction, after forming **Fe^{1+}** species

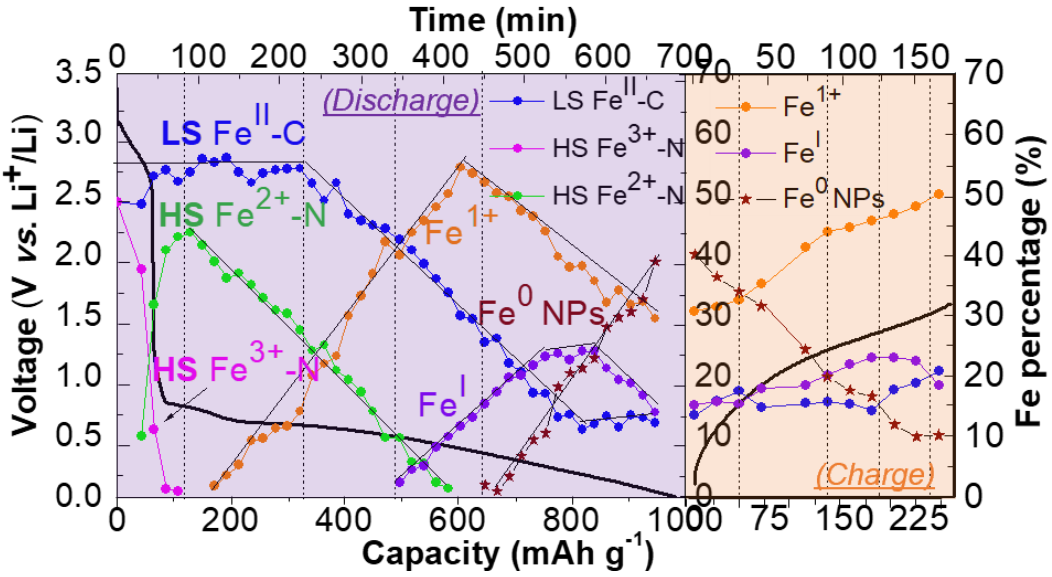

Please see the reduced “8,25 cm x 4,45 cm” version below:

Prussian blue undergoes a conversion reaction, after forming **Fe^{1+}** species